GEOPHYSICS, VOL. 84, NO. 4 (JULY-AUGUST 2019); P. S329–S340, 24 FIGS., 1 TABLE.
10.1190/GEO2018-0391.1

Check for updates

Downloaded 09/14/19 to 138.67.129.106. Redistribution subject to SEG license or copyright; see Terms of Use at http://library.seg.org/

Least-squares Gaussian beam migration in elastic media

Yubo Yue[1], Paul Sava[2], Zhongping Qian[1], Jidong Yang[3], and Zhen Zou[1]

ABSTRACT

Gaussian beam migration (GBM) is an effective imaging method that has the ability to image multiple arrivals while preserving the advantages of ray-based methods. We have extended this method to linearized least-squares imaging for elastic waves in isotropic media. We have dynamically transformed the multicomponent data to the principal components of different wave modes using the polarization information available in the beam migration process, and then we use Gaussian beams as wavefield propagator to construct the forward modeling and adjoint migration operators. Based on the constructed operators, we formulate a least-squares migration scheme that is iteratively solved using a preconditioned conjugate gradient method. With this method, we can obtain crosstalk-attenuated multiwave images with better subsurface illumination and higher resolution than those of the conventional elastic Gaussian beam migration. This method also allows us to achieve a good balance between computational cost and imaging accuracy, which are both important requirements for iterative least-squares migrations. Numerical tests on two synthetic data sets demonstrate the validity and effectiveness of our proposed method.

INTRODUCTION

Depth migration is an important step of multicomponent data processing. A common procedure for migrating multicomponent data in practice is to assume that downward propagation from the source location occurs as P-waves, which are reflected as either P-waves or S-waves to be recorded by multicomponent receivers. Then, treating the z-component data as P-waves and the radial-components as PS-waves and migrating them separately using acoustic methods. However, this approach suffers from (1) crosstalk noise caused by directly migrating the coupled elastic waves and (2) inaccurate imaging polarity for converted-wave imaging because polarity reversal is no longer at the zero offset when the P/S velocity ratio varies (Rosales and Rickett, 2001). To make full use of the vector wavefields and obtain high-quality multiwave images, we should approach this problem using elastic imaging methods.

Elastic Kirchhoff migration (EKM) is typically used for migrating multicomponent data (Kuo and Dai, 1984; Hokstad, 2000). This technique computes traveltime and polarization information for PP- and PS-waves via ray tracing, and it sums the vector data along traveltime trajectories. EKM offers a high level of efficiency. However, it suffers from the limitations of classic ray theory, including amplitude singularity in caustic regions and difficulties for imaging multiple arrivals (Gray et al., 2001). Another kind of elastic migration method is elastic reverse time migration (ERTM) (Yan and Sava, 2008; Du et al., 2012, 2017; Duan and Sava, 2015), in which a numerical solution to the elastic-wave equation is used to extrapolate the P- and S-wave wavefields simultaneously, followed by wave mode separation during the imaging process. Although ERTM has high imaging accuracy, its computational efficiency is low, which significantly hinders its practical application. Gaussian beam migration (GBM) is an elegant imaging method (Hill, 1990, 2001; Hale, 1992; Gray, 2005; Nowack et al., 2005; Gao et al., 2006; Gray and Bleistein, 2009; Yue et al., 2012, 2019a, 2019b) because it not only preserves the high efficiency of ray-based migration methods, but it also achieves high level of accuracy by migrating multipath arrivals. Recently, Protasov and Tcheverda (2012), Li et al. (2018), and Yang et al. (2018a) successfully extend GBM to elastic isotropic media, providing a competitive alternative to imaging elastic waves.

Least-squares migration (LSM) seeks a reflectivity model that can predict data consistent with the observed data (Nemeth et al., 1999; Duquet et al., 2000; Zeng et al., 2014; Zhang et al., 2015). It is used to compensate for acquisition noise, poor sampling of sources and receivers on the surface, as well as poor illumination

Manuscript received by the Editor 20 May 2018; revised manuscript received 16 December 2018; published ahead of production 19 March 2019; published online 30 May 2019.
[1]Bureau of Geophysical Prospecting Inc., R&D Center, Zhuozhou, China. E-mail: geoyyb@163.com (corresponding author), qianzhongping@cnpc.com.cn; zouzhen@cnpc.com.cn.
[2]Colorado School of Mines, Center for Wave Phenomena, Golden, Colorado, USA. E-mail: psava@mines.edu.
[3]The University of Texas at Dallas, Geosciences Department, Richardson, Texas, USA. E-mail: jidong.yang.china@gmail.com.
© 2019 Society of Exploration Geophysicists. All rights reserved.

Downloaded 09/14/19 to 138.67.129.106. Redistribution subject to SEG license or copyright; see Terms of Use at http://library.seg.org/

of the subsurface. LSM can be implemented using the Kirchhoff integral (Nemeth et al., 1999; Duquet et al., 2000) or wave-equation propagators (Zeng et al., 2014; Zhang et al., 2015). Hu et al. (2016) and Yang et al. (2018b) show that LSM can also be effectively implemented using Gaussian beams. For imaging elastic waves, the existing elastic LSM (ELSM) methods are mainly implemented with the two-way wave propagator (Duan et al., 2017; Feng and Schuster, 2017). However, because the computational cost of one iteration of ELSM is twice that of conventional ERTM, the expense of all ELSM iterations is often prohibitively high in large-scale applications.

To provide an efficient approach of ELSM, we propose elastic least-squares Gaussian beam migration (ELSGBM), which can not only produce better illuminated elastic images with enhanced resolution and attenuated crosstalk, but it can also achieve a good balance between computational cost and imaging accuracy. Instead of using vector Gaussian beams to extrapolate the elastic wavefields with Cartesian components (Protasov and Tcheverda 2012; Li et al., 2018; Yang et al., 2018a), we choose an equivalent but simpler approach by extrapolating principal component wavefields using scalar wave propagators (Goertz, 2002; Schleicher et al., 2007; Stolt and Weglein, 2012), which is helpful in constructing the conjugate modeling and migration operators. We dynamically transform multicomponent data to the principal components of different wave modes using the polarization vectors available in the migration process, and then we use scalar Gaussian beams as the wave propagator to construct the forward modeling and the adjoint migration operators. Based on the constructed operators, we formulate LSM for elastic waves and use a preconditioned conjugate gradient (Nemeth et al., 1999) to iteratively solve for the optimal images.

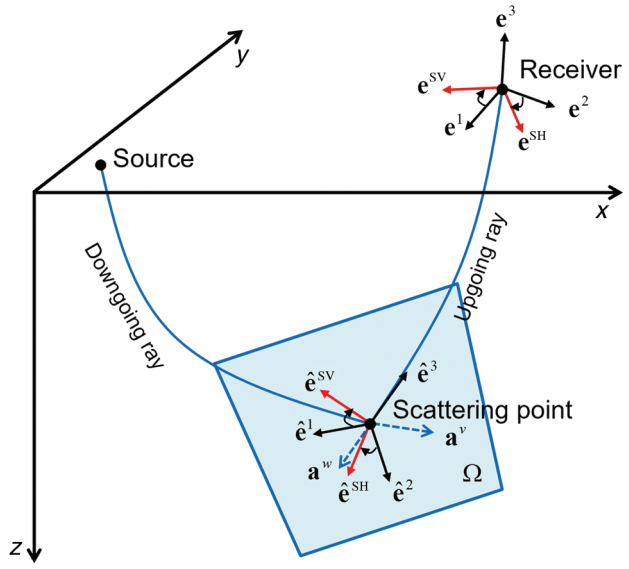


Figure 1. Schematic diagram showing the determination of polarization vectors $\mathbf{e}^{\mathrm{SV}}, \mathbf{e}^{\mathrm{SH}}$ at the receiver location. After ray tracing, $\hat{\mathbf{e}}^1, \hat{\mathbf{e}}^2, \hat{\mathbf{e}}^3$ and $\mathbf{e}^1, \mathbf{e}^2, \mathbf{e}^3$, which are unit vectors of the ray-centered coordinate system at the scattering point and the receiver location, respectively, can be obtained, and the plane of incidence Ω can be defined by the source ray slowness vector $\mathbf{a}^v$ and the receiver ray slowness vector $\mathbf{a}^w$. We rotate $\hat{\mathbf{e}}^1, \hat{\mathbf{e}}^2$ about $\hat{\mathbf{e}}^3$ to be $\hat{\mathbf{e}}^{\mathrm{SV}}, \hat{\mathbf{e}}^{\mathrm{SH}}$ which are parallel and perpendicular to the plane Ω, respectively, and then we apply the same rotation angle to $\mathbf{e}^1, \mathbf{e}^2$ to obtain the polarization vectors $\mathbf{e}^{\mathrm{SV}}, \mathbf{e}^{\mathrm{SH}}$ at the receiver location.

To verify the validity and effectiveness of the method, we use two synthetic data sets and show that ELSGBM is capable of producing elastic images with high resolution and balanced amplitudes and suppressing crosstalk noise caused by the coupled elastic waves.

METHOD

We assume a 3D elastic and smoothly inhomogeneous isotropic medium with a free-space acquisition surface. The multicomponent data $\mathbf{u}(\mathbf{x}_r, \mathbf{x}_s, \omega)$ recorded at receiver $\mathbf{x}_r$ are generated by an omnidirectional point source with coordinate $\mathbf{x}_s$. In the derivations, we use superscripts to denote the wave modes and subscripts to denote the Cartesian components of elastic waves. There is no summation on the repeated indices throughout this paper.

Principal components of elastic waves

According to the zero-order ray theory (Červený, 2001), we can use three mutually orthogonal, right-handed unit vectors $\mathbf{e}^1, \mathbf{e}^2, \mathbf{e}^3$ of the ray-centered coordinate system to represent the polarization vectors of the principal components of S1-waves, S2-waves, and P-waves, respectively. Although $\mathbf{e}^3$ is always perpendicular to the wavefront, unit vectors $\mathbf{e}^1, \mathbf{e}^2$ can be arbitrarily rotated about $\mathbf{e}^3$.

Considering the ray from the receiver location (see Figure 1), if we rotate the unit vector $\hat{\mathbf{e}}^1, \hat{\mathbf{e}}^2$ at the scattering point about $\hat{\mathbf{e}}^3$ and particularly make $\hat{\mathbf{e}}^1$ parallel to the plane of incidence defined by source and receiver ray slowness vectors, then the rotated $\hat{\mathbf{e}}^1$ and $\hat{\mathbf{e}}^2$ become the polarization vectors of SV- and SH-waves (denoted as $\hat{\mathbf{e}}^{\mathrm{SV}}, \hat{\mathbf{e}}^{\mathrm{SH}}$ in Figure 1), respectively. With this particular choice, the S1- and S2-waves (now as SV- and SH-waves) are fully decoupled and the matrix of reflection coefficients in isotropic elastic media simplifies to five nonzero components, instead of nine (Červený, 2001; Goertz, 2002). We can apply the same rotation process to the unit vectors $\mathbf{e}^1, \mathbf{e}^2, \mathbf{e}^3$ at the receiver location to obtain the polarization vectors $\mathbf{e}^{\mathrm{SV}}, \mathbf{e}^{\mathrm{SH}}, \mathbf{e}^{\mathrm{P}}$ and use them to transform the recorded multicomponent data $\mathbf{u}(\mathbf{x}_r, \mathbf{x}_s, \omega)$ to the three principal components $u^{\mathrm{SV}}, u^{\mathrm{SH}}, u^{\mathrm{P}}$ of elementary SV-waves, SH-waves, and P-waves by

$$\begin{pmatrix} u^{\mathrm{SV}} \\ u^{\mathrm{SH}} \\ u^{\mathrm{P}} \end{pmatrix} = \mathbf{H}^T \begin{pmatrix} u_x \\ u_y \\ u_z \end{pmatrix}, \tag{1}$$

where

$$\mathbf{H} = (\mathbf{e}^{\mathrm{SV}}, \mathbf{e}^{\mathrm{SH}}, \mathbf{e}^{\mathrm{P}}) = \begin{pmatrix} e_x^{\mathrm{SV}} & e_x^{\mathrm{SH}} & e_x^{\mathrm{P}} \\ e_y^{\mathrm{SV}} & e_y^{\mathrm{SH}} & e_y^{\mathrm{P}} \\ e_z^{\mathrm{SV}} & e_z^{\mathrm{SH}} & e_z^{\mathrm{P}} \end{pmatrix}, \tag{2}$$

denotes the transformation matrix from the ray-centered coordinate system to the Cartesian coordinate system at the receiver location. Because the matrix depends on the rotation process, which varies with different scattering points, this transformation must be dynamically implemented during the modeling or migration process. After this transformation, each principal component can be considered as scalarized elastic wavefields and extrapolated by a scalar wavefield operator (Jackson et al., 1991; Takahashi, 1995; Goertz, 2002; Lüth et al., 2005; Schleicher et al., 2007). Based on this idea, we derive the forward modeling and migration operators of elastic waves using the scalar Green's function in the following sections.

Downloaded 09/14/19 to 138.67.129.106. Redistribution subject to SEG license or copyright; see Terms of Use at http://library.seg.org/

Elastic wave Born modeling formula

With the notated assumptions, we can apply the linearized single-scattering theory (Aki and Richards, 2002; Stolt and Weglein, 2012) to derive the elastic wave Born modeling formula. For a source generating omnidirectional downgoing waves with wave mode v, the recorded principal component wavefields $u^w(\mathbf{x}_r, \mathbf{x}_s, \omega)$ with upgoing wave mode w can be represented as

$$u^w(\mathbf{x}_r,\mathbf{x}_s,\omega) = \mathbf{e}^w(\mathbf{x},\mathbf{x}_s)\cdot\mathbf{u}(\mathbf{x}_r,\mathbf{x}_s,\omega) = \omega^2\int d\mathbf{x}F(\omega)G^w(\mathbf{x},\mathbf{x}_r,\omega)M^{wv}(\mathbf{x})G^v(\mathbf{x},\mathbf{x}_s,\omega), \tag{3}$$

where $F(\omega)$ is the source wavelet, $M^{wv}(\mathbf{x})$ is the scattering potential at scattering point $\mathbf{x}$, $G^w(\mathbf{x},\mathbf{x}_r,\omega)$ is the upgoing scalar Green's function with wave mode w, and $G^v(\mathbf{x},\mathbf{x}_s,\omega)$ is the downgoing scalar Green's function with wave mode v. After taking account of all possible down- and upgoing wave modes, we can write the forward modeling formula in operator form:

$$\mathbf{u}(\mathbf{x}_r,\mathbf{x}_s,\omega) = \omega^2\int d\mathbf{x}F(\omega)\mathbf{H}\mathbf{G}(\mathbf{x},\mathbf{x}_r,\omega)\mathbf{M}(\mathbf{x})\mathbf{G}(\mathbf{x},\mathbf{x}_s,\omega), \tag{4}$$

where $\mathbf{H}$ is the transformation matrix defined in equation 2 and $\mathbf{M}(\mathbf{x})$ is the scattering potential matrix that has five nonzero components

$$\mathbf{M}(\mathbf{x}) = \begin{pmatrix} M^{\mathrm{SVSV}} & 0 & M^{\mathrm{SVP}} \\ 0 & M^{\mathrm{SHSH}} & 0 \\ M^{\mathrm{PSV}} & 0 & M^{\mathrm{PP}} \end{pmatrix}, \tag{5}$$

where $\mathbf{G}(\mathbf{x},\mathbf{x}_r,\omega)$ is the 3×3 diagonal matrix of the upgoing Green's functions

$$\mathbf{G}(\mathbf{x},\mathbf{x}_r,\omega) = \mathrm{diag}(G^{\mathrm{SV}}, G^{\mathrm{SH}}, G^{\mathrm{P}}), \tag{6}$$

and $\mathbf{G}(\mathbf{x},\mathbf{x}_s,\omega)$ is the 3×1 column matrix of the downgoing Green's functions

$$\mathbf{G}(\mathbf{x},\mathbf{x}_s,\omega) = (G^{\mathrm{SV}}, G^{\mathrm{SH}}, G^{\mathrm{P}})^T. \tag{7}$$

Elastic wave Gaussian beam Born modeling

The choice of Green's function in equations 6 and 7 determines the Born modeling method. Instead of choosing the classic ray solution, which results in conventional ray-Born modeling (Červený and Coppoli, 1992), we express the Green's function as a summation of Gaussian beams, which can easily account for multipathing and ensure nonsingular amplitudes. With the derivations in Appendix A, we arrive at the elastic Gaussian beam Born (EGB) modeling formula as a sum over sparsely spaced beam center locations L:

$$u_m(\mathbf{x}_r,\mathbf{x}_s,\omega) = -\Phi\sum_w\sum_v\sum_{\mathbf{L}}\iint\frac{dp_x^w dp_y^w}{p_z^w} \times U_m^{wv}(\mathbf{L},\mathbf{x}_s,\mathbf{p}^w,\omega) \times\exp\left[-i\omega\mathbf{p}^w\cdot(\mathbf{x}_r-\mathbf{L}) - \left|\frac{\omega}{\omega_r}\right|\frac{|\mathbf{x}_r-\mathbf{L}|^2}{2w_0^2}\right], \tag{8}$$

where $u_m(\mathbf{x}_r,\mathbf{x}_s,\omega)$ represents the modeled multicomponent data, Φ is a frequency-dependent term defined in equation A-9, $\mathbf{L}$ represents the beam center location with spacing $\Delta\mathbf{L}$, $\mathbf{p} = (p_x, p_y, p_z)^T$ is the initial ray parameter vector of the central ray at the surface, and ω_r and w_0 are the reference frequency and initial half-width of Gaussian beams (Hill, 1990, 2001), respectively. The term $U_m^{wv}(\mathbf{L},\mathbf{x}_s,\mathbf{p}^w,\omega)$ represents the modeled m-component plane waves for the upgoing wave mode w and downgoing wave mode v, and it is expressed as

$$U_m^{wv}(\mathbf{L},\mathbf{x}_s,\mathbf{p}^w,\omega) = \iint\frac{dp_x^v dp_y^v}{p_z^v}\int d\mathbf{x}F(\omega) \times e_m^w(\mathbf{x},\mathbf{L})M^{wv}(\mathbf{x})[A_R^{wv}(\mathbf{L},\mathbf{x}_s) + iA_I^{wv}(\mathbf{L},\mathbf{x}_s)] \times\exp[i\omega\tau_R^{wv}(\mathbf{L},\mathbf{x}_s) - \omega\tau_I^{wv}(\mathbf{L},\mathbf{x}_s)], \tag{9}$$

where $e_m^w(\mathbf{x},\mathbf{L})$ is the polarization vector of the upgoing waves at the beam center location and the amplitudes A_R^{wv}, A_I^{wv} and traveltimes τ_R^{wv}, τ_I^{wv} are defined in equation A-5.

The summation in equation 8 accumulates the modeled multimode plane waves at each beam center to the nearby receiver wavefields. It implies an inverse slant stack operation, which can be efficiently implemented in frequency-wavenumber domain. Equation 9 represents a combined smearing and convolution process, which is computed in the time domain to ensure efficiency.

Computational steps of EGB modeling

The workflow of EGB modeling for simulating a multicomponent shot gather can be summarized as follows:

1) Prepare smoothed velocities and determine the necessary modeling parameters such as the beam initial width, ray parameter spacing, and beam center spacing (Hill, 1990, 2001).
2) For a source with wave mode v, trace the central rays from the source location with different initial ray parameters and save the calculated beam tables for repeated use in the iterative LSM process.
3) For a selected upgoing wave mode w, calculate and save the receiver beam tables at each beam center location as in step 2.
   a) For each beam center $\mathbf{L}$, loop over the source and receiver beam pairs.
      I) Calculate $e_m^w(\mathbf{x},\mathbf{L})$ and other quantities in equation 9 for each scattering point $\mathbf{x}$ in the aperture illuminated by source and receiver beams.
      II) Smear the scattering amplitude $M^{wv}(\mathbf{x})$ onto the temporary multicomponent tau-p panels by evaluating equation 9.
   b) After repeating step a for all beam centers, convolve the temporary tau-p panels with the source wavelet to produce

Downloaded 09/14/19 to 138.67.129.106. Redistribution subject to SEG license or copyright; see Terms of Use at http://library.seg.org/

the modeled multicomponent local plane waves $U_m^{wv}(\mathbf{L}, \mathbf{x}_s, \mathbf{p}^w, \omega)$.

c) Accumulate the local plane waves at each beam center to the nearby receivers by evaluating equation 8 to obtain the multicomponent data corresponding to the selected upgoing wave mode.

4) Repeat step 3 for other upgoing wave modes and add the results together, then the final multicomponent shot gather $u_m(\mathbf{x}_r, \mathbf{x}_s, t)$ simulated by EGB modeling is obtained.

Adjoint elastic Gaussian beam migration

Elastic migration is defined as the adjoint operator of forward modeling. From equation 3, we can write the shot domain migration formula as

$$M^{wv}(\mathbf{x}) = \int d\omega \int d\mathbf{x}_r \omega^2 F^*(\omega) G^{w*}(\mathbf{x}, \mathbf{x}_r, \omega) \times [\mathbf{e}^w(\mathbf{x}, \mathbf{x}_r) \cdot \mathbf{u}(\mathbf{x}_r, \mathbf{x}_s, \omega)] G^{v*}(\mathbf{x}, \mathbf{x}_s, \omega), \quad (10)$$

where superscript $*$ denotes the complex conjugate. Here, we also use the summation of Gaussian beams to calculate the Green's function. By inserting equation A-1 into equation 10, we have

$$M^{wv}(\mathbf{x}) = -\frac{\omega^4}{4\pi^2} \int d\omega \int d\mathbf{x}_r \omega^2 F^*(\omega) \times \iint \frac{dp_x^w dp_y^w}{p_z^w} \iint \frac{dp_x^v dp_y^v}{p_z^v} \times [A_R^{wv}(\mathbf{x}_r, \mathbf{x}_s) - iA_I^{wv}(\mathbf{x}_r, \mathbf{x}_s)] \times \exp[-i\omega\tau_R^{wv}(\mathbf{x}_r, \mathbf{x}_s) - \omega\tau_I^{wv}(\mathbf{x}_r, \mathbf{x}_s)] \times [\mathbf{e}^w(\mathbf{x}, \mathbf{x}_r) \cdot \mathbf{u}(\mathbf{x}_r, \mathbf{x}_s, \omega)]. \quad (11)$$

To accelerate migrations, we apply the same strategies as in equations A-6 and A-7, and we arrive at the final expression of elastic Gaussian beam migration (EGBM):

$$M^{wv}(\mathbf{x}) = -\sum_{\mathbf{L}} \int d\omega \iint \frac{dp_x^w dp_y^w}{p_z^w} \iint \frac{dp_x^v dp_y^v}{p_z^v} \times [A_R^{wv}(\mathbf{L}, \mathbf{x}_s) - iA_I^{wv}(\mathbf{L}, \mathbf{x}_s)] D^w(\mathbf{L}, \mathbf{p}^w, \omega) \times \exp[-i\omega\tau_R^{wv}(\mathbf{L}, \mathbf{x}_s) - \omega\tau_I^{wv}(\mathbf{L}, \mathbf{x}_s)], \quad (12)$$

where $D^w(\mathbf{L}, \mathbf{p}^w, \omega)$ is the tapered slant stack of the principal component of the selected wave mode w:

$$D^w(\mathbf{L}, \mathbf{p}^w, \omega) = \Phi F^*(\omega) \times \int d\mathbf{x}_r [\mathbf{e}^w(\mathbf{x}, \mathbf{L}) \cdot \mathbf{u}(\mathbf{x}_r, \mathbf{x}_s, \omega)] \times \exp\left[i\omega\mathbf{p}^w \cdot (\mathbf{x}_r - \mathbf{L}) - \left|\frac{\omega}{\omega_r}\right| \frac{|\mathbf{x}_r - \mathbf{L}|^2}{2w_0^2}\right]. \quad (13)$$

Equations 12 and 13 are asymptotically equivalent to the EGBM formulas of Li et al. (2018) derived using vector Gaussian beams (their equations 18 through 20, with free-space surface condition A-11), which also confirms our proposed scalar beam approach to extrapolating principal components of elastic waves.

The implementation of EGBM is similar to that of conventional GBM, except for the dot-product operation in equation 13, which represents a model-driven elastic wave mode separation that projects the multicomponent data recorded at receiver location $\mathbf{x}_r$ onto the expected polarization vector approximately evaluated at beam center location $\mathbf{L}$. This operation extracts the pure wavefields corresponding to a given wave mode and simultaneously suppresses crosstalk with other wave modes. Moreover, this operation also ensures correct imaging polarity for converted waves. If the velocity model is accurate enough, the modeled polarity is similar to the polarity contained in the data, and thus the dot-product produces a positive projection.

Least-squares migration

ELSGBM aims to find the multiwave images that best predict, in a least-squares sense, the

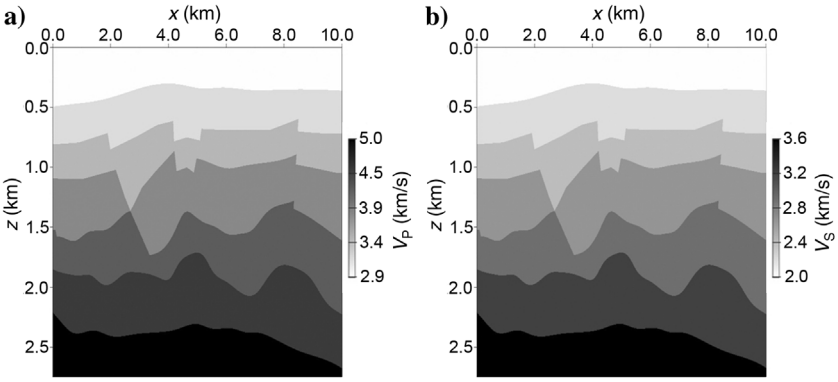


Figure 2. A synthetic multi-layer model. (a) P-wave velocity model and (b) S-wave velocity model.

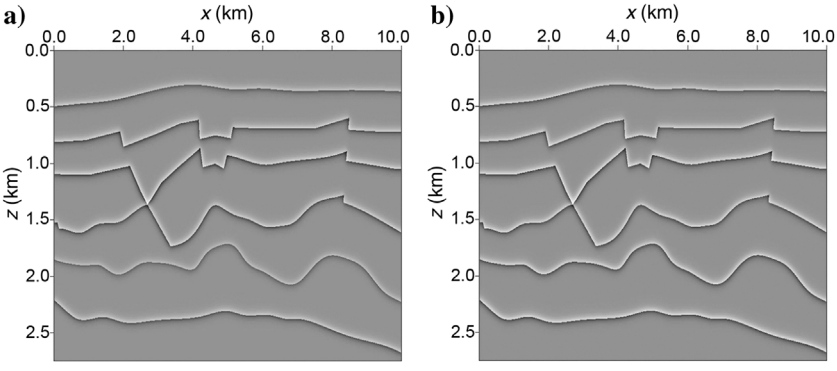


Figure 3. Multiwave scattering potentials. (a) PP-scattering potential and (b) PS-scattering potential.

Downloaded 09/14/19 to 138.67.129.106. Redistribution subject to SEG license or copyright; see Terms of Use at http://library.seg.org/

recorded multicomponent seismic data. ELSGBM is implemented in the shot domain, and its misfit function is built using the l_2 norm of residuals between the modeled and recorded multicomponent data:

$$J = \frac{1}{2}\|\mathbf{Lm}\text{-}\mathbf{d}\|^2, \tag{14}$$

where $\mathbf{m}$ is the prestack multiwave images defined in equation 5, $\mathbf{d}$ is the recorded multicomponent data, and $\mathbf{L}$ is the EGB modeling operator whose adjoint is defined as $\mathbf{L}^T$. We compute the multiwave gradients using multicomponent data residuals, and we use a preconditioned conjugate gradient method (Nemeth et al., 1999) to simultaneously update the images:

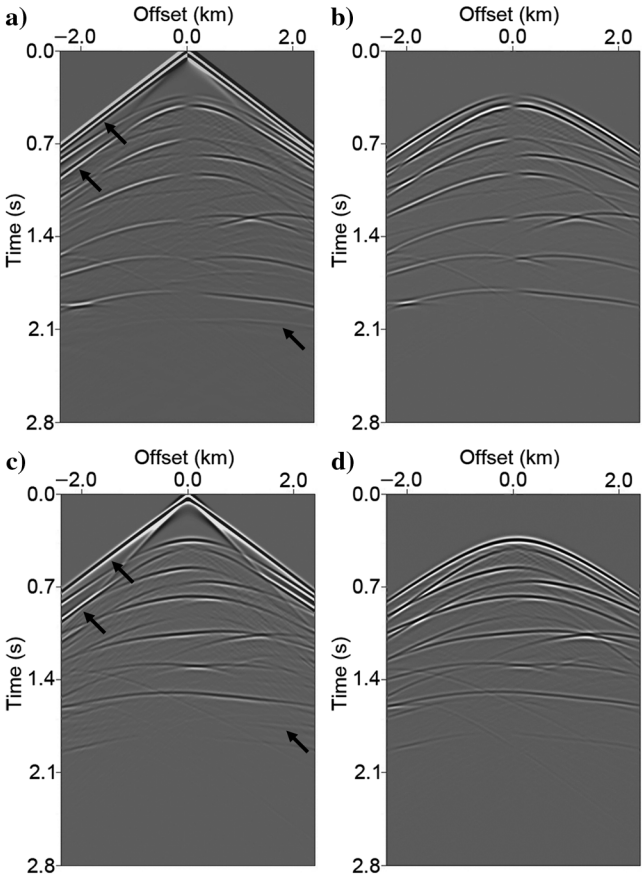


Figure 4. Synthetic shot gathers at $x = 2.0$ km generated using different elastic modeling methods. The black arrows indicate the events that are not accounted for in EGB modeling. (a) FD-modeled x-component data, (b) EGB-modeled x-component data, (c) FD-modeled z-component data, and (d) EGB-modeled z-component data.

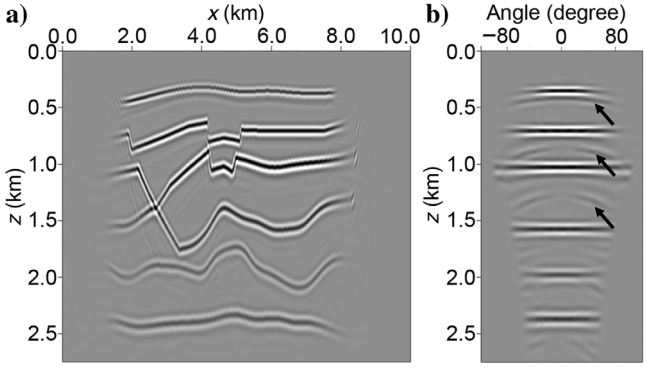


Figure 5. Acoustic Gaussian beam migration results with arrows indicating the PS crosstalk. (a) PP-image and (b) PP-ADCIG at $x = 6.0$ km.

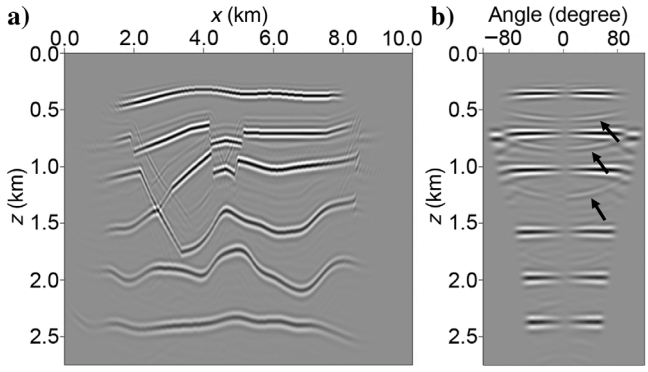


Figure 6. Acoustic Gaussian beam migration results with arrows indicating the PP crosstalk. (a) PS-image and (b) PS-ADCIG at $x = 6.0$ km.

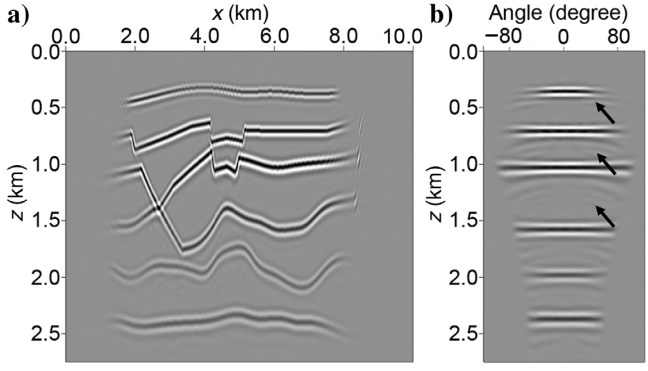


Figure 7. Elastic Gaussian beam migration (the adjoint operator) results with arrows indicating the attenuated PS crosstalk. (a) PP-image and (b) PPADCIG at $x = 6.0$ km.

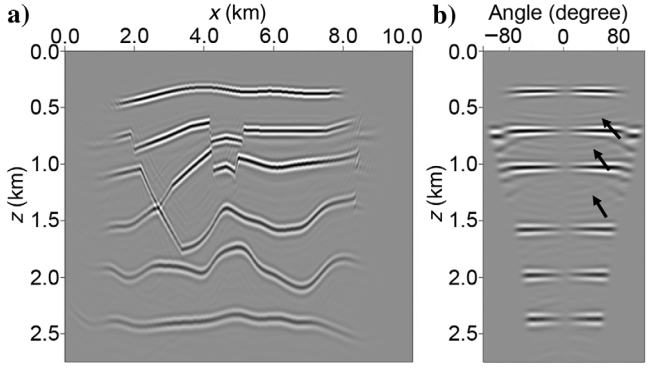


Figure 8. Elastic Gaussian beam migration results with arrows indicating the attenuated PP crosstalk. (a) PS-image and (b) PS-ADCIG at $x = 6.0$ km.

$$\mathbf{m}^{(k+1)} = \mathbf{m}^{(k)} - \alpha \mathbf{dk}^{(k)}, \tag{15}$$

where $\mathbf{dk}^{(k)}$ is the revised conjugate gradient direction of the kth iteration and α is the corresponding step length. They can be calculated with the following equations:

$$\mathbf{dk}^{(k)} = \mathbf{Cg}^{(k)} + \beta \mathbf{dk}^{(k-1)}, \tag{16}$$

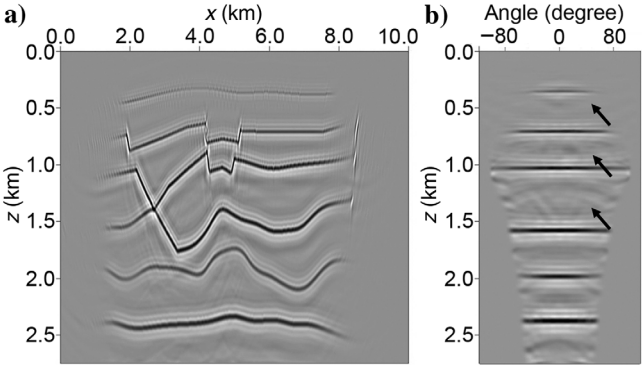


Figure 9. Elastic least-squares Gaussian beam migration results with arrows indicating the nearly eliminated PS crosstalk. (a) PP-image and (b) PP-ADCIG at $x = 6.0$ km.

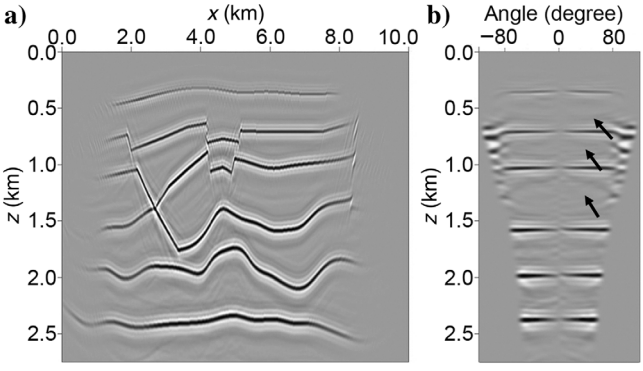


Figure 10. Elastic least-squares Gaussian beam migration results with arrows indicating the nearly eliminated PP crosstalk. (a) PS-image and (b) PS-ADCIG at $x = 6.0$ km.

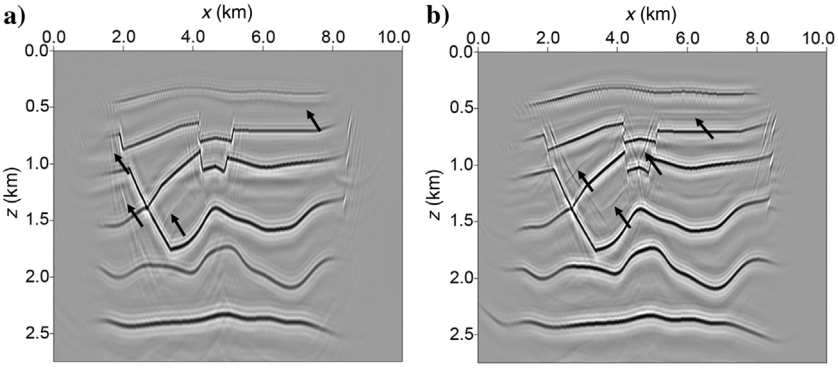


Figure 11. Acoustic least-squares Gaussian beam migration results with arrows indicating the crosstalk artifacts. (a) PP-image and (b) PS-image.

$$\alpha = \frac{(\mathbf{dk}^{(k)})^T \mathbf{g}^{(k)}}{(\mathbf{Lk}^{(k-1)})^T (\mathbf{Ldk}^{(k-1)})}, \tag{17}$$

where preconditioner $\mathbf{C}$ is the inverse of diagonal Hessian (Plessix and Mulder, 2004; Yang et al., 2018b) and is used to accelerate the convergence. We can efficiently use beam tables to compute the diagonal Hessian on the coarse grid and then interpolate it onto the fine imaging grid. The terms $\mathbf{g}^{(k)}$ and β are the gradients and step length of the kth iteration, respectively, using the steepest-descent method, which are expressed as

$$\mathbf{g}^{(k)} = \mathbf{L}^T(\mathbf{Lm}^{(k)} - \mathbf{d}), \tag{18}$$

$$\beta = \frac{(\mathbf{g}^{(k)})^T (\mathbf{Cg}^{(k)})}{(\mathbf{g}^{(k-1)})^T (\mathbf{Cg}^{(k-1)})}. \tag{19}$$

EXAMPLES

The effectiveness of ELSGBM is now demonstrated with two synthetic examples: (1) a multilayer model and (2) a modified Marmousi2 model. We compute multiwave images using different beam migration algorithms and compare them to demonstrate the improvements in the image resolution and illumination of ELSGBM. We also extract angle-domain common image gathers (ADCIGs), which are indexed by migration opening angle and easily implemented using ray-angle information available in beam migrations, to show the suppression of crosstalk after ELSGBM. In addition, we verify the efficiency advantage of ELSGBM by comparing the computational cost between EGB modeling and finite-difference (FD) modeling.

Multilayer model

We first demonstrate the advantages of ELSGBM using a multilayer model, whose grid size is 1000 × 550 with lateral spacing 10 m and vertical spacing 5 m. The P- and S-wave velocities are shown in Figure 2a and 2b, respectively, and they are smoothed using a damped least-squares algorithm (Popov et al., 2010) to meet the requirement of ray-tracing as well as ray-Born modeling. We use an $O(2, 8)$ staggered-grid FD solver of elastic wave equation to generate 200 multicomponent shot gathers using an explosive P-wave source with a 20 Hz Ricker wavelet and a nonfree measurement surface. The shot spacing is 30 m, and each shot gather has 241 receivers with 20 m spacing. We also compute the same data using EGB modeling with the multiwave scattering potentials shown in Figure 3 to compare with the FD-modeled results and verify the simulation accuracy. The modeled x- and z-component data are shown in Figure 4a–4d, respectively. We can see that the multicomponent data produced by EGB modeling are similar to the FD-modeled results, except the direct waves, multiples, and wide-angle reflections, which are not accounted for in EGB modeling (marked by the black arrows). The comparisons show that EGB modeling is an accurate method to simulate the first-order elastic waves.

Downloaded 09/14/19 to 138.67.129.106. Redistribution subject to SEG license or copyright; see Terms of Use at http://library.seg.org/

Downloaded 09/14/19 to 138.67.129.106. Redistribution subject to SEG license or copyright; see Terms of Use at http://library.seg.org/

We test migration algorithms on the FD-modeled data, whose first arrivals are muted in advance using a linear mute function, to demonstrate the advantages of ELSGBM. First, we use acoustic Gaussian beam migration (AGBM) to migrate the z-component data to produce approximate PP-imaging results and the polarity-reversed x-component data to produce approximate PS-imaging results (reversing the polarity of the data with a negative offset and using the S-wave velocity to compute the receiver beams), shown in Figures 5 and 6, respectively. Although AGBM correctly recovers subsurface structures in the PP- and PS-images (Figures 5a and 6a), migrating single-component data using AGBM causes strong crosstalk (marked by the black arrows) in the extracted ADCIGs (Figures 5b and 6b), which results from migrating the coupled elastic wavefields using unmatched velocities. The crosstalk may be partially attenuated in the AGBM stacked image (Figures 5a and 6a), but its nonflat appearance in ADCIGs inevitably complicates the velocity updating. We next use the proposed ELSGBM to migrate the x- and z-component data. The imaging results after one iteration (known as adjoint EGBM) are shown in Figures 7 and 8. We can see that EGBM produces similar stacked images (Figures 7a and 8a) as AGBM, but the crosstalk noise is significantly attenuated in ADCIGs due to the dot-product operation (equation 13) embedded in EGBM (Figures 7b and 8b). Figures 9 and 10 show the PP- and PS-imaging results after 15 iterations of ELSGBM. Compared with AGBM and EGBM, ELSGBM generates improved resolution and more balanced illumination and the extracted ADCIGs are almost free of crosstalk noise. To demonstrate the superiority of ELSGBM over conventional acoustic LSM, we compute the PP- and PS-images using acoustic least-squares Gaussian beam migration (ALSGBM), and they are shown in Figure 11a and 11b, respectively. We can see that ALSGBM images show apparent crosstalk noise emerging as false structures (marked by the black arrows).

Next, we calculate the spectra of the EGBM and ELSGBM images shown in Figure 12. We find that the ELSGBM images (the red curves) have a broader bandwidth at the high and low wavenumbers, indicating their higher resolution than the EGBM images (the blue curves). The source wavelet has a great impact on the overall imaging quality of LSM. For real data, it can be estimated using the full Newton method in the frequency domain (Kim et al., 2011) or a designature process (Vigh and Starr, 2008). We also show the multicomponent data residuals after 15 iterations and the normalized objective function versus number of iterations in Figures 13 and 14, respectively. Compared with the original FD-modeled multicomponent data shown in Figure 4a and 4c, most of the

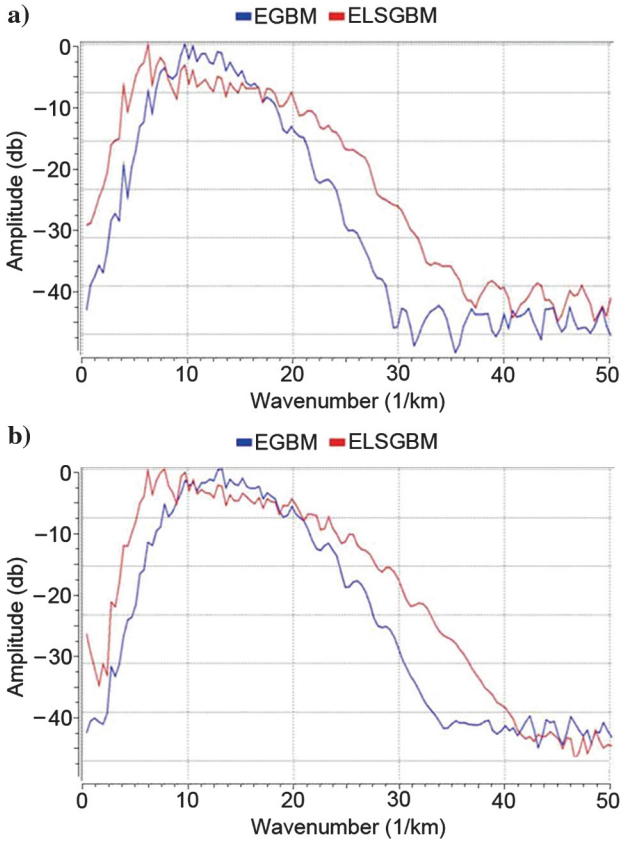


Figure 12. Spectrum comparisons between the local EGBM and ELSGBM images located from 3.0 to 6.0 km in the x-direction and from 0.5 to 2.5 km in the z-direction. (a) PP-image comparison and (b) PS-image comparison.

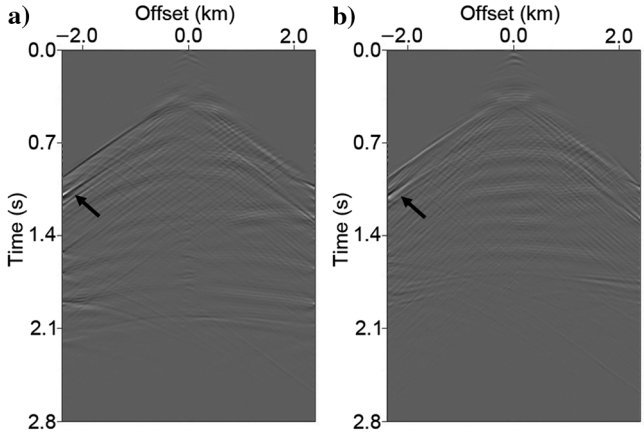


Figure 13. Data residuals after 15 iterations of ELSGBM (plotted on the same scale as the FD-modeled data shown in Figure 4). The strong data residuals indicated by the black arrows are wide-angle reflections which cannot be modeled using EGB modeling. Panel (a) shows x-component data residual and (b) shows z-component data residual.

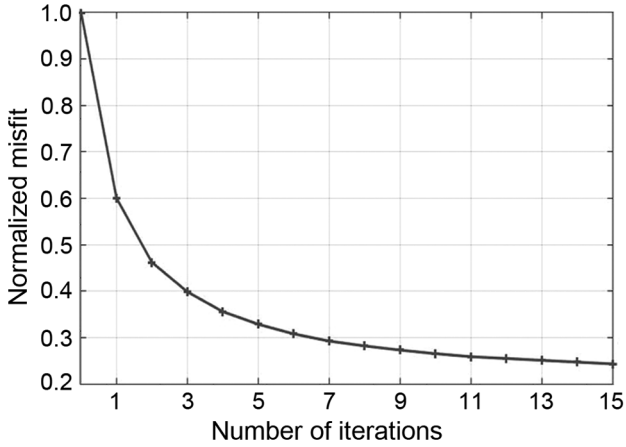


Figure 14. Normalized objective function versus iterations for ELSGBM on the multilayer model example.

multicomponent data residuals are eliminated after ELSGBM, except the wide-angle reflections with complex-valued coefficients (marked by the black arrows in Figure 13), which are not accounted for in our current algorithm.

Marmousi2 model

We use a modified Marmousi2 model (Martin et al., 2006) to verify the effectiveness of our proposed ELSGBM with complex structures. Figure 15a shows the P-wave velocity model with the water layer replaced by a solid medium; the S-wave velocity shown in Figure 15b is a scaled version of the P-wave velocity with V_P/V_S ratios ranging from 3.1 to 1.6. A total of 240 multicomponent shot gathers are simulated using the same FD elastic wave equation solver with 40 m source spacing, one of which is shown in Figure 16. The explosive P-wave source uses a Ricker wavelet with 20 Hz peak frequency. For each shot, there are 351 receivers evenly distributed around the source location with a 20 m spacing.

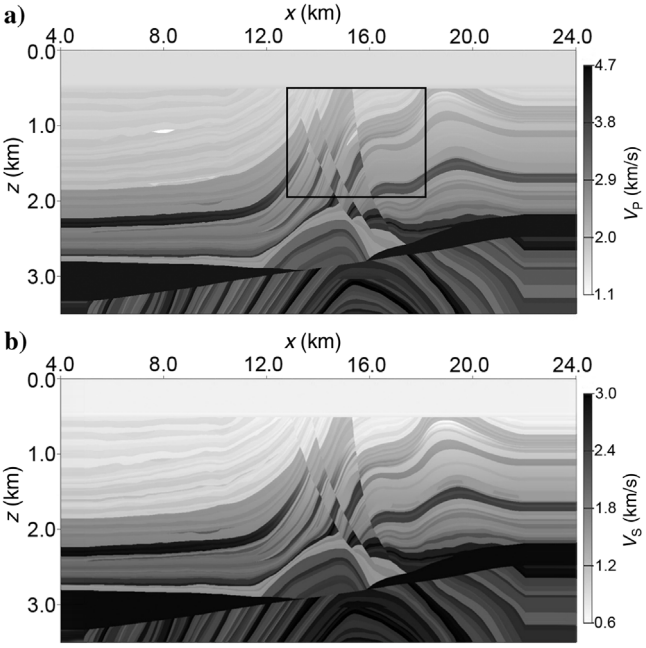


Figure 15. Marmousi2 velocity models with the black box indicating an area for imaging comparison. (a) P-wave velocity model and (b) S-wave velocity model.

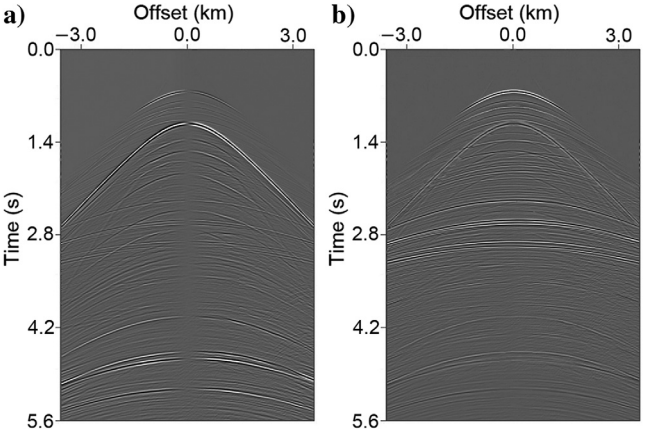


Figure 16. Synthetic multi-component shot gathers at $x = 7.0$ km generated using FD modeling. Panel (a) shows x-component data and (b) shows z-component data. Note that we have muted the first arrivals.

The EGBM results after one iteration are shown in Figures 17 and 18, and the ELSGBM results after 20 iterations are shown in Figures 19 and 20, respectively. Although EGBM is capable of accurately recovering the complex Marmousi2 structures in the PP- and PS-images (Figures 18a and 19a), the illumination and resolution of the central steep reflectors are poor. In contrast, ELSGBM produces images and ADCIGs with more balanced illumination and higher resolution (Figures 19 and 20). The magnified views of the true scattering potentials of the Marmousi2 model for the box marked in Figure 15a, as well as the EGBM and ELSGBM stacked images, are shown in Figure 21. The PP- and PS-stacked images have good consistency with the true scattering potentials, especially for the hydrocarbon reservoirs (marked by the white boxes) and the zero

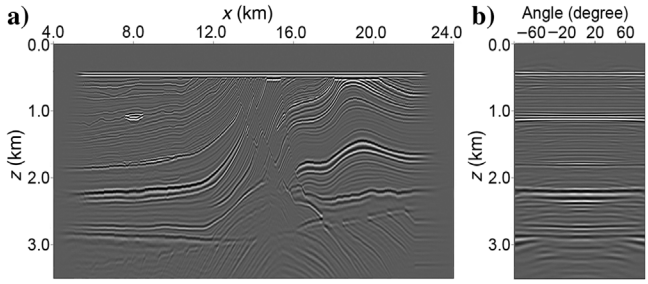


Figure 17. Elastic Gaussian beam migration. (a) PP-image and (b) PP-ADCIG at $x = 8.0$ km.

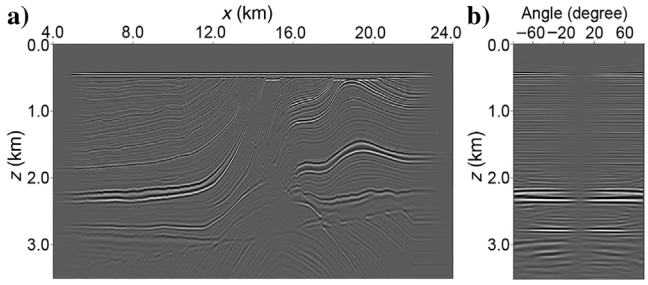


Figure 18. Elastic Gaussian beam migration. (a) PS-image and (b) PS-ADCIG at $x = 8.0$ km.

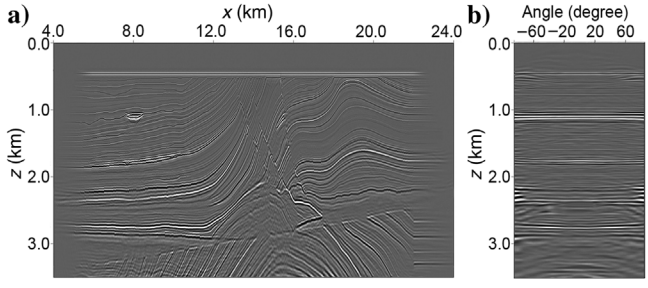


Figure 19. Elastic least-squares Gaussian beam migration. (a) PP-image and (b) PP-ADCIG at $x = 8.0$ km.

Downloaded 09/14/19 to 138.67.129.106. Redistribution subject to SEG license or copyright; see Terms of Use at http://library.seg.org/

Downloaded 09/14/19 to 138.67.129.106. Redistribution subject to SEG license or copyright; see Terms of Use at http://library.seg.org/

P-wave impedance sand (marked by the white arrows), which are helpful features when inverting for elastic parameters. Compared with the EGBM results, ELSGBM improves the image amplitudes and continuity of steeply dipping structures, and it reveals the thin-layered structures (the black arrows). The improved resolution is confirmed by the spectrum comparison shown in Figure 22, in which the spectra of the ELSGBM images (the red curves) are wider than that of EGBM images. The multicomponent data residuals after ELSGBM are shown in Figure 23, and the corresponding convergence curve is shown in Figure 24. After 20 iterations of ELSGBM, most of the recorded PP- and PS-data residuals are eliminated (the initial data residual is shown in Figure 16), demonstrating the effectiveness of our proposed method.

Computational cost

Because the costs of forward modeling and migration in one LSM iteration are similar, it is fair to compare the computational time between EGB modeling and FD modeling to verify the efficiency advantage of ELSGBM. In the implementation of EGB modeling, we follow the criterion proposed by Hill (2001) to choose beam parameters such as the initial width and ray parameter spacing, and we use the steepest-descent approximation (Hill, 2001; Gray and Bleistein, 2009) to reduce the computational loads of forward modeling (equations 8 and 9) and migration (equations 11 and 12).

The computational time of one shot gather using these two modeling algorithms is shown in Table 1. We can see that EGB modeling is more than 50 times faster than FD modeling in these two models with relatively high S-wave velocity, and the efficiency advantage of ELSGBM is further enhanced if we choose models with a lower S-wave velocity or a source wavelet with a higher peak frequency. For example, if we reduce the S-wave velocity by a factor of N, then the grid spacing and time step of FD modeling are also required to be reduced by a factor of N to avoid numerical dispersion, which means that the computational cost will be increased by N^3 times in these 2D examples. As for EGB modeling, the reduced S-wave velocity leads to a smaller initial width for the S-wave beams, but it does not change the overall cost too much.

DISCUSSION

Because the earth is an elastic medium and seismic energy propagating inside the earth is in the form of elastic waves, applying elastic migrations to the recorded multicomponent data should be the optimal way to reveal geologic structures and extract elastic properties. However, there are several challenges preventing the successful application of the existing full elastic imaging method:

1) Low S-wave velocities (sometimes on the order of 100 m/s), which necessitate small spacing of receivers and migration grid, especially for seafloor data. The current receiver spacing, even for land data, is not often fine enough to capture unaliased wavefields at usable frequencies, and the fine computational grid often imposes a prohibitive expense on the elastic wave-equation imaging method such as ERTM (Duan et al., 2017).

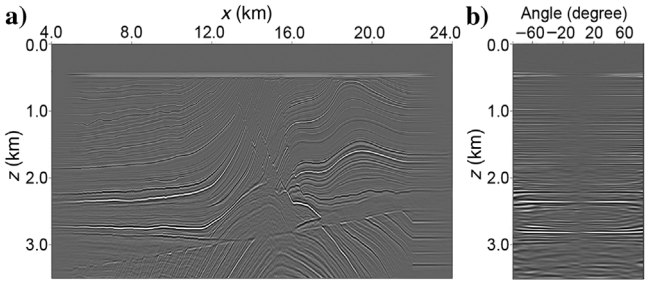


Figure 20. Elastic least-squares Gaussian beam migration. (a) PS-image and (b) PS-ADCIG at $x = 8.0$ km.

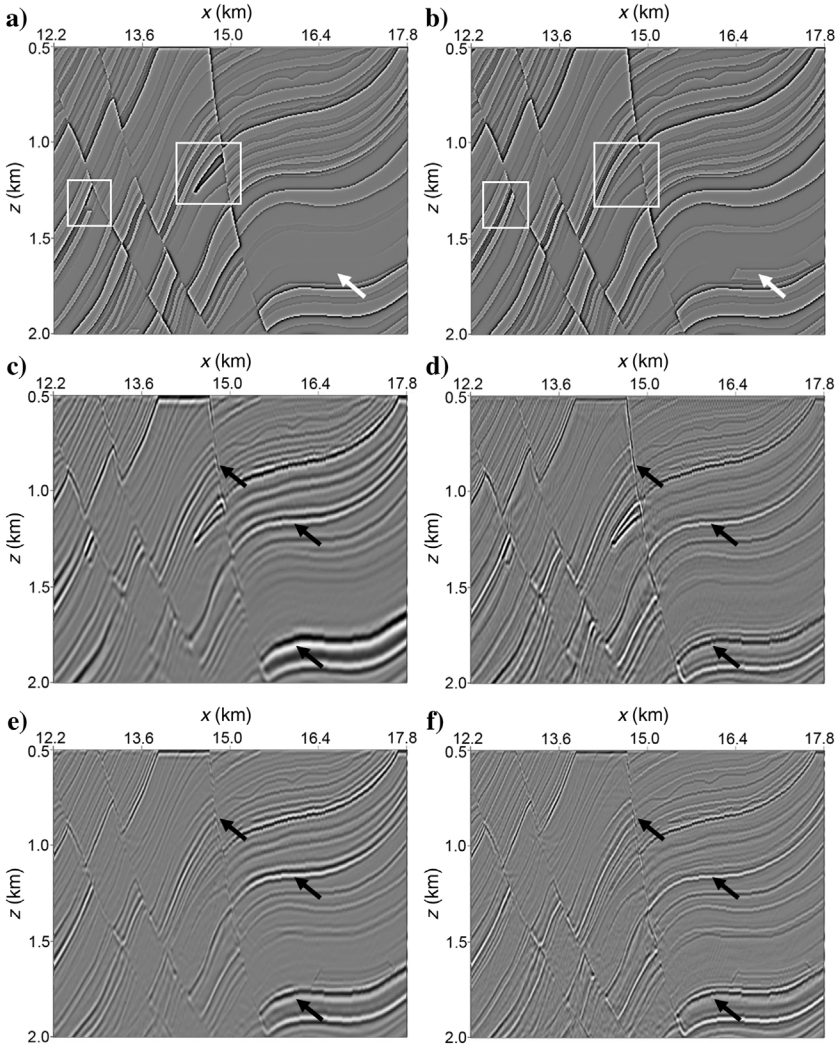


Figure 21. Magnified views of the box shown in Figure 15 for the images in Figures 17 through 20. (a) PP-scattering potential, (b) PS-scattering potential, (c) PP-EGBM image, (d) PP-ELSGBM image, (e) PS-EGBM image, and (f) PS-ELSGBM image.

Downloaded 09/14/19 to 138.67.129.106. Redistribution subject to SEG license or copyright; see Terms of Use at http://library.seg.org/

2) Velocity anisotropy causes triplicated traveltimes especially for S-waves, which result in discontinuities in the single-valued traveltime tables of standard EKM and thus lead to the noisy character of migrated images (Casasanta and Gray, 2015). This also poses a challenge for the efficient and accurate implementation of wavefield separation in ERTM (Yan and Sava, 2011).

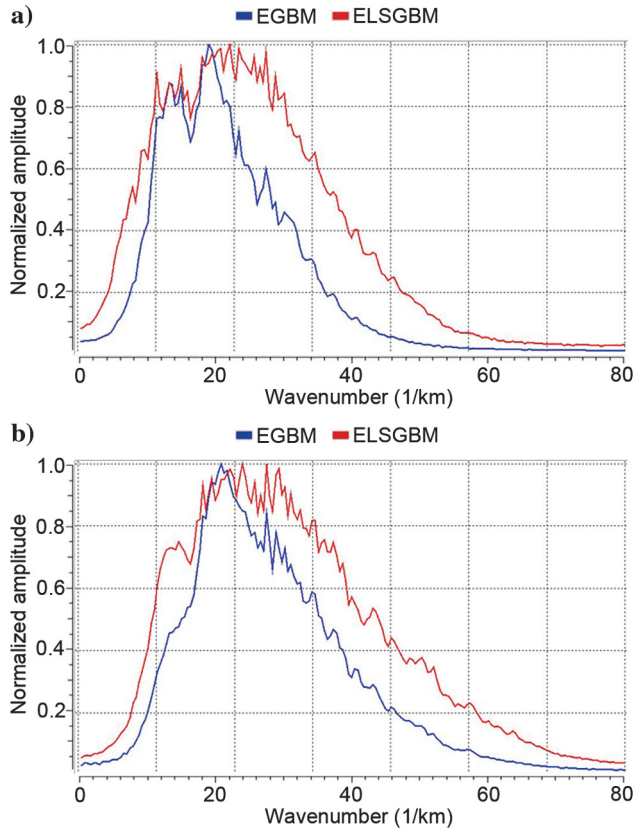


Figure 22. Spectrum comparisons between EGBM and ELSGBM images shown in Figure 21. (a) PP-image comparison and (b) PS-image comparison.

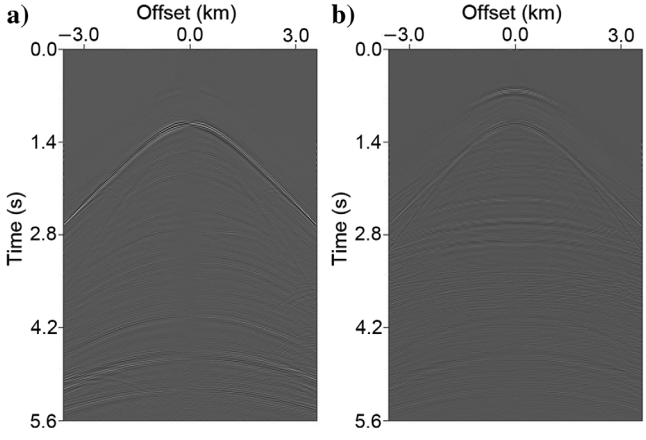


Figure 23. Data residuals after 20 iterations of ELSGBM (plotted on the same scale as the original data shown in Figure 16). Panel (a) shows x-component data residual and (b) shows z-component data residual.

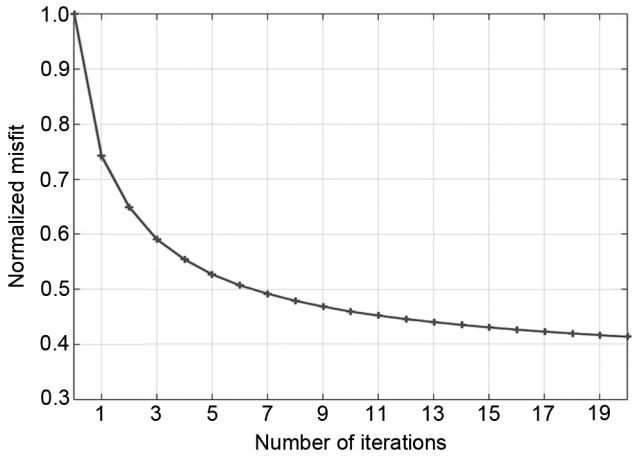


Figure 24. Normalized objective function versus iterations for ELSGBM on the Marmousi2 example.

Table 1. Comparisons of computational time between different elastic modeling algorithms.

	EGB modeling	FD modeling
Multilayer model	3.1 s	162.5 s
Marmousi2 model	17.7 s	1359.2 s

3) Seismic attenuation of S-waves is more severe than that of P-waves, partially negating the promise of higher PS-image resolution.
4) The processing steps before migration should be applied with the same parameter configuration to each single-component data so as to maintain the vector information contained in the multicomponent data. In addition, an accurate elastic model building is a necessity for elastic migration but still poses a challenge.

EGBM may, to some extent, mitigate the first two problems mentioned above. First, the fine grid spacing requirements of ERTM can be relaxed in EGBM due to migration antialiasing (Gray, 2013). Second, strong S-wave anisotropy and triplications can be handled in EGBM (Casasanta and Gray, 2015) to a large extent. Third, elastic wave polarizations can be tracked using the method shown in Figure 1 and thus used to separate the elastic wavefields. As an extension of EGBM, the proposed ELSGBM keeps the merits of EGBM while providing crosstalk-attenuated images with better illumination and higher resolution.

At present, the proposed method is limited to isotropic elastic media, in which S-wave polarizations are much simpler than in anisotropic media; future work will focus on incorporating anisotropy into the method.

CONCLUSION

We proposed an ELSGBM method for elastic waves in isotropic media. By using Gaussian beams as wave propagator to formulate the LSM scheme, we achieved high-resolution images while preserving the high computational efficiency and accuracy. Our method operates

Downloaded 09/14/19 to 138.67.129.106. Redistribution subject to SEG license or copyright; see Terms of Use at http://library.seg.org/

by extracting the principal components of the multicomponent data, which enable us to suppress crosstalk and ensure accurate polarity for converted wave imaging. Trials on two synthetic data sets show that our proposed method produces multiwave images with higher resolution and better illumination compared with conventional acoustic or elastic Gaussian beam migrations.

ACKNOWLEDGMENTS

We thank the Bureau of Geophysical Prospecting for permission to publish this paper. We are grateful to the assistant editor E. Gasperikova, the associate editor J. Schleicher, S. Gray, and three anonymous reviews for their insightful suggestions and comments. The research was jointly funded by the Scientific Research and Technology Development Project of CNPC (grant no. 2018D-5010-06), the National Nature Science Foundation of China (grant nos. 41874164 and 41874168), and the Young Elite Scientists Sponsorship program by CAST (grant no. YESS20160127).

DATA AND MATERIALS AVAILABILITY

Data associated with this research are available and can be obtained by contacting the corresponding author.

APPENDIX A

ELASTIC WAVE GAUSSIAN BEAM BORN MODELING

In the appendix, we derive an asymptotic solution for elastic Born modeling using the Green's function expressed in terms of Gaussian beams.

The Green's function $G^u(\mathbf{x},\mathbf{x}',\omega)$ of one wave mode u can be represented by the summation of Gaussian beams connecting the scattering point $\mathbf{x}$ and the surface point $\mathbf{x}'$

$$G^u(\mathbf{x},\mathbf{x}',\omega)=\frac{i\omega}{2\pi}\iint\frac{dp_x^u dp_y^u}{p_z^u}A^u(\mathbf{x},\mathbf{x}')\times\exp[i\omega\tau^u(\mathbf{x},\mathbf{x}')], \tag{A-1}$$

where $\mathbf{p}^u=(p_x,p_y,p_z)^T$ is the initial ray parameter vector of the central ray at the surface. The terms $A^u(\mathbf{x},\mathbf{x}')$ and $\tau^u(\mathbf{x},\mathbf{x}')$ are the complex amplitude and traveltime, respectively (Červený, 2001), in the following forms:

$$A^u(\mathbf{x},\mathbf{x}')=A_R^u(\mathbf{x},\mathbf{x}')+iA_I^u(\mathbf{x},\mathbf{x}'), \tag{A-2}$$

$$\tau^u(\mathbf{x},\mathbf{x}')=\tau_R^u(\mathbf{x},\mathbf{x}')+i\tau_I^u(\mathbf{x},\mathbf{x}'), \tag{A-3}$$

where the subscripts R and I represent the real and imaginary parts of the complex quantities, respectively. By inserting equation A-1 into equation 4, we can express the elastic wave Born modeling formula in terms of the Gaussian beams:

$$\begin{aligned}u_m(\mathbf{x}_r,\mathbf{x}_s,\omega)=&-\frac{\omega^4}{4\pi^2}\sum_w\sum_v\iint\frac{dp_x^w dp_y^w}{p_z^w}\\&\times\iint\frac{dp_x^v dp_y^v}{p_z^v}\int d\mathbf{x}F(\omega)\\&\times e_m^w(\mathbf{x},\mathbf{x}_r)M^{wv}(\mathbf{x})[A_R^{wv}(\mathbf{x}_r,\mathbf{x}_s)+iA_I^{wv}(\mathbf{x}_r,\mathbf{x}_s)]\\&\times\exp[i\omega\tau_R^{wv}(\mathbf{x}_r,\mathbf{x}_s)-\omega\tau_I^{wv}(\mathbf{x}_r,\mathbf{x}_s)],\end{aligned} \tag{A-4}$$

where m represents the Cartesian components of the modeled multicomponent data, superscripts w and v represent the up- and downgoing wave modes, respectively. The terms $A_R^{wv}(\mathbf{x}_r,\mathbf{x}_s)$ and $A_I^{wv}(\mathbf{x}_r,\mathbf{x}_s)$ are the real and imaginary parts of the product of the source and receiver beam complex amplitudes, respectively, and $\tau_R^{wv}(\mathbf{x}_r,\mathbf{x}_s)$ and $\tau_I^{wv}(\mathbf{x}_r,\mathbf{x}_s)$ are the real and imaginary parts of the sum of source and receiver beam complex traveltimes, respectively. These quantities have the following expressions:

$$\begin{aligned}A_R^{wv}(\mathbf{x}_r,\mathbf{x}_s)&=A_R^w(\mathbf{x},\mathbf{x}_r)A_R^v(\mathbf{x},\mathbf{x}_s)-A_I^w(\mathbf{x},\mathbf{x}_r)A_I^v(\mathbf{x},\mathbf{x}_s),\\A_I^{wv}(\mathbf{x}_r,\mathbf{x}_s)&=A_R^w(\mathbf{x},\mathbf{x}_r)A_I^v(\mathbf{x},\mathbf{x}_s)+A_I^w(\mathbf{x},\mathbf{x}_r)A_R^v(\mathbf{x},\mathbf{x}_s),\\\tau_R^{wv}(\mathbf{x}_r,\mathbf{x}_s)&=\tau_R^w(\mathbf{x},\mathbf{x}_r)+\tau_R^v(\mathbf{x},\mathbf{x}_s),\\\tau_I^{wv}(\mathbf{x}_r,\mathbf{x}_s)&=\tau_I^w(\mathbf{x},\mathbf{x}_r)+\tau_I^v(\mathbf{x},\mathbf{x}_s).\end{aligned} \tag{A-5}$$

To accelerate the computation of equation A-4, we trace beams at coarse beam center locations $\mathbf{L}$ instead of the dense receiver locations (Hill, 2001; Gray and Bleistein, 2009) and we use them to approximately calculate the receiver wavefields by incorporating a phase shift $\exp[-i\omega\mathbf{p}^w\cdot(\mathbf{x}_r-\mathbf{L})]$

$$G^w(\mathbf{x},\mathbf{x}_r,\omega)=\frac{i\omega}{2\pi}\iint\frac{dp_x^w dp_y^w}{p_z^w}A^w(\mathbf{x},\mathbf{L})\times\exp[i\omega\tau^w(\mathbf{x},\mathbf{L})-i\omega\mathbf{p}^w\cdot(\mathbf{x}_r-\mathbf{L})]. \tag{A-6}$$

To reduce the error of this acceleration process, we apply a partition of unity (Hill, 1990; Bleistein, 2009; Gray and Bleistein, 2009) to equation A-4:

$$\frac{\sqrt{3}}{4\pi}\left|\frac{\omega}{\omega_r}\right|\left(\frac{\Delta\mathbf{L}}{w_0}\right)\sum_{\mathbf{L}}\exp\left[-\left|\frac{\omega}{\omega_r}\right|\frac{|\mathbf{x}_r-\mathbf{L}|^2}{2w_0^2}\right]\approx 1 \tag{A-7}$$

and arrive at the final Born modeling formula:

$$\begin{aligned}u_m(\mathbf{x}_r,\mathbf{x}_s,\omega)=&-\Phi\sum_w\sum_v\sum_{\mathbf{L}}\iint\frac{dp_x^w dp_y^w}{p_z^w}\\&\times U_m^{wv}(\mathbf{L},\mathbf{x}_s,\mathbf{p}^w,\omega)\\&\times\exp\left[-i\omega\mathbf{p}^w\cdot(\mathbf{x}_r-\mathbf{L})-\left|\frac{\omega}{\omega_r}\right|\frac{|\mathbf{x}_r-\mathbf{L}|^2}{2w_0^2}\right],\end{aligned} \tag{A-8}$$

where

$$\Phi=\frac{\sqrt{3}\omega^4}{16\pi^3}\left|\frac{\omega}{\omega_r}\right|\left(\frac{\Delta\mathbf{L}}{w_0}\right), \tag{A-9}$$

where $\Delta\mathbf{L}$ is the beam center spacing and ω_r and w_0 are the selected reference frequency and initial half-width of Gaussian beams, respectively. The term $U_m^{wv}(\mathbf{L},\mathbf{x}_s,\mathbf{p}^w,\omega)$ represents the modeled plane waves of the m-component for the upgoing wave mode w and downgoing wave mode v, and it is expressed as

$$U_m^{wv}(\mathbf{L},\mathbf{x}_s,\mathbf{p}^w,\omega)=\int\int\frac{dp_x^v dp_y^v}{p_z^v}\int d\mathbf{x}F(\omega)\times e_m^w(\mathbf{x},\mathbf{L})M^{wv}(\mathbf{x})[A_R^{wv}(\mathbf{L},\mathbf{x}_s)+iA_I^{wv}(\mathbf{L},\mathbf{x}_s)]\times\exp[i\omega\tau_R^{wv}(\mathbf{L},\mathbf{x}_s)-\omega\tau_I^{wv}(\mathbf{L},\mathbf{x}_s)]. \quad \text{(A-10)}$$

REFERENCES

Aki, K., and P. G. Richards, 2002, Quantitative seismology, 2nd ed.: University Science Books.

Bleistein, N., 2009, Mathematics of modeling, migration and inversion with Gaussian beams: Center for Wave Phenomena, Colorado School of Mines.

Casasanta, L., and S. H. Gray, 2015, Converted-wave beam migration with sparse sources or receivers: Geophysical Prospecting, **63**, 534–551, doi: 10.1111/1365-2478.12226.

Červený, V., 2001, Seismic ray theory: Cambridge University Press.

Červený, V., and D. Coppoli, 1992, Ray-Born synthetic seismograms for complex structures containing scatters: Journal of Seismic Exploration, **1**, 191–206.

Du, Q., C. Guo, Q. Zhao, X. Gong, C. Wang, and X. Li, 2017, Vector based elastic reverse time migration based on acoustic imaging condition: Geophysics, **82**, no. 2, S111–S127, doi: 10.1190/geo2016-0146.1.

Du, Q., Y. Zhu, and J. Ba, 2012, Polarity reversal correction for elastic reverse time migration: Geophysics, **77**, no. 2, S31–S41, doi: 10.1190/geo2011-0348.1.

Duan, Y., and P. Sava, 2015, Scalar imaging condition for elastic reverse time migration: Geophysics, **80**, no. 4, S127–S136, doi: 10.1190/geo2014-0453.1.

Duan, Y., P. Sava, and A. Guitton, 2017, Elastic least-squares reverse time migration: Geophysics, **82**, no. 4, S315–S325, doi: 10.1190/geo2016-0564.1.

Duquet, B., K. J. Marfurt, and J. A. Dellinger, 2000, Kirchhoff modeling, inversion for reflectivity, and subsurface illumination: Geophysics, **65**, 1195–1209, doi: 10.1190/1.1444812.

Feng, Z., and G. T. Schuster, 2017, Elastic least-squares reverse time migration: Geophysics, **82**, no. 2, S143–S157, doi: 10.1190/geo2016-0254.1.

Gao, F., P. Zhang, B. Wang, and V. Dirks, 2006, Fast beam migration — A step toward interactive imaging: 76th Annual International Meeting, SEG, Expanded Abstracts, 2470–2474, doi: 10.1190/1.2370032.

Goertz, A., 2002, True-amplitude multicomponent migration of elastic wavefields: Ph.D. dissertation, University of Karlsruhe.

Gray, S. H., 2005, Gaussian beam migration of common-shot records: Geophysics, **70**, no. 4, S71–S77, doi: 10.1190/1.1988186.

Gray, S. H., 2013, Spatial sampling, migration aliasing, and migrated amplitudes: Geophysics, **78**, no. 3, S157–S164, doi: 10.1190/geo2012-0451.1.

Gray, S. H., and N. Bleistein, 2009, True-amplitude Gaussian-beam migration: Geophysics, **74**, no. 2, S11–S23, doi: 10.1190/1.3052116.

Gray, S. H., J. Etgen, J. Dellinger, and D. Whitmore, 2001, Seismic migration problems and solutions: Geophysics, **66**, 1622–1640, doi: 10.1190/1.1487107.

Hale, D., 1992, Migration by the Kirchhoff, slant stack, and Gaussian beam methods: Report 121, Colorado School of Mines, Center for wave phenomena.

Hill, N. R., 1990, Gaussian beam migration: Geophysics, **55**, 1416–1428, doi: 10.1190/1.1442788.

Hill, N. R., 2001, Prestack Gaussian-beam depth migration: Geophysics, **66**, 1240–1250, doi: 10.1190/1.1487071.

Hokstad, K., 2000, Multicomponent Kirchhoff migration: Geophysics, **65**, 861–873, doi: 10.1190/1.1444783.

Hu, H., Y. Liu, Y. Zheng, X. Liu, and H. Lu, 2016, Least-squares Gaussian beam migration: Geophysics, **81**, no. 3, S87–S100, doi: 10.1190/geo2015-0328.1.

Jackson, G. M., I. M. Mason, and D. Lee, 1991, Multicomponent common-receiver gather migration of single-level walk-away seismic profiles: Geophysical Prospecting, **39**, 1015–1029.

Kim, Y., D. J. Min, and C. Shin, 2011, Frequency-domain reverse-time migration with source estimation: Geophysics, **76**, no. 2, S41–S49, doi: 10.1190/1.3534831.

Kuo, J., and T. Dai, 1984, Kirchhoff elastic wave migration for the case of noncoincident source and receiver: Geophysics, **49**, 1223–1238, doi: 10.1190/1.1441751.

Li, X., W. Mao, X. Shi, and Y. Yue, 2018, Elastic 3D PS converted-wave Gaussian beam migration: Geophysics, **83**, no. 3, S213–S225, doi: 10.1190/geo2017-0122.1.

Lüth, S., S. Buske, R. Giese, and A. Goertz, 2005, Fresnel volume migration of multicomponent data: Geophysics, **70**, no. 6, S121–S129, doi: 10.1190/1.2127114.

Martin, G. S., R. Wiley, and K. J. Marfurt, 2006, Marmousi2: An elastic upgrade for Marmousi: The Leading Edge, **25**, 156–166.

Nemeth, T., C. Wu, and G. T. Schuster, 1999, Least-squares migration of incomplete reflection data: Geophysics, **64**, 208–221, doi: 10.1190/1.1444517.

Nowack, R. L., M. K. Sen, and P. L. Stoffa, 2005, Gaussian beam migration for sparse common-shot and common-receiver data: 75th Annual International Meeting, SEG, Expanded Abstracts, 1114–1117, doi: 10.1190/1.1817470.

Plessix, R. E., and W. A. Mulder, 2004, Frequency-domain finite-difference amplitude-preserving migration: Geophysical Journal International, **157**, 975–987.

Popov, M. M., N. M. Semtchenok, P. M. Popov, and A. R. Verdel, 2010, Depth migration by the Gaussian beam summation method: Geophysics, **75**, no. 2, S81–S93, doi: 10.1190/1.3361651.

Protasov, M., and V. Tcheverda, 2012, True amplitude elastic Gaussian beam imaging of multicomponent walkaway vertical seismic profiling data: Geophysical Prospecting, **60**, 1030–1042, doi: 10.1111/j.1365-2478.2012.01068.x.

Rosales, D., and J. Rickett, 2001, PS-wave polarity reversal in angle domain common-image gathers: 71st Annual International Meeting, SEG, Expanded Abstracts, 1843–1846, doi: 10.1190/1.1816489.

Schleicher, J., M. Tygel, and P. Hubral, 2007, Seismic true-amplitude imaging: SEG, Geophysical Development Series 12.

Stolt, R. H., and A. B. Weglein, 2012, Seismic imaging and inversion: Application of linear inverse theory: Cambridge University Press.

Takahashi, T., 1995, Prestack migration using arrival angle information: Geophysics, **60**, 154–163, doi: 10.1190/1.1443742.

Vigh, D., and E. W. Starr, 2008, 3D prestack plane-wave, full-waveform inversion: Geophysics, **73**, no. 5, VE135–VE144, doi: 10.1190/1.2952623.

Yan, J., and P. Sava, 2008, Isotropic angle-domain elastic reverse-time migration: Geophysics, **73**, no. 6, S229–S239, doi: 10.1190/1.2981241.

Yan, J., and P. Sava, 2011, Improving the efficiency of elastic wave-mode separation for heterogeneous tilted transverse isotropic media: Geophysics, **76**, no. 4, T65–T78, doi: 10.1190/geo2017-0078.1.

Yang, J., H. Zhu, J. Huang, and Z. Li, 2018a, 2D isotropic elastic Gaussian-beam migration for common-shot multicomponent records: Geophysics, **83**, no. 2, S127–S140, doi: 10.1190/geo2017-0078.1.

Yang, J., H. Zhu, G. McMechan, and Y. Yue, 2018b, Time-domain least-squares migration using the Gaussian beam summation method: Geophysical Journal International, **214**, 548–572, doi: 10.1093/gji/ggy142.

Yue, Y., Z. Li, Z. Qian, J. Zhang, P. Sun, and G. Ma, 2012, Amplitude-preserved Gaussian beam migration under complex topographic conditions: Chinese Journal of Geophysics, **55**, 1376–1383.

Yue, Y., Z. Qian, X. Zhang, D. Wang, Y. Yue, and W. Chang, 2019a, Gaussian beam based Born modeling method for single-scattering waves in acoustic medium: Chinese Journal of Geophysics, **62**, 648–656.

Yue, Y., P. Sun, D. Wang, P. Sun, Z. Guo, and Z. Liu, 2019b, Gaussian beam based modeling method for single-scattering waves in elastic isotropic medium: Chinese Journal of Geophysics, **62**, 657–666.

Zeng, C., S. Dong, and B. Wang, 2014, Least-squares reverse time migration: Inversion-based imaging toward true reflectivity: The Leading Edge, **33**, 962–964, doi: 10.1190/tle33090962.1.

Zhang, Y., L. Duan, and Y. Xie, 2015, A stable and practical implementation of least-squares reverse time migration: Geophysics, **80**, no. 1, V23–V31, doi: 10.1190/geo2013-0461.1.

Downloaded 09/14/19 to 138.67.129.106. Redistribution subject to SEG license or copyright; see Terms of Use at http://library.seg.org/